ACS OMEGA

http://pubs.acs.org/journal/acsodf
Article

Surface Reconstruction of Single-Twinned AgPdIr Nanoalloy during the Formate Oxidation and Dehydrogenation Reactions

Quan Tang, Longfei Guo, Tao Jin, Shuang Shan, Qiao Wang, Junpeng Wang, Bowei Pan, Zhen Li, and Fuyi Chen*

Cite This: ACS Omega 2024, 9, 45811−45821
Read Online

ABSTRACT: Formate has emerged as a promising energy carrier to generate electrons via formate oxidation reaction (FOR) and hydrogen via formate dehydrogenation reaction (FDR), and it is desirable but difficult to design a novel bifunctional (electro)catalyst to improve reaction kinetics. Herein, we construct the single-twinned AgPdIr (t-AgPdIr) nanoalloy to improve the catalytic activity and stability for the formate oxidation and dehydrogenation processes. The t-AgPdIr nanoalloy, characterized by a distinctive twinned structure with strains and a downshift of the d-band center, demonstrates an improved peak current density of 4.6 A·mg_{Pd}^{-1}, a diminished onset potential of 0.45 V, a superior activity retention of 55.7% after 600 cycles, and a current density of 0.73 A·mg_{Pd}^{-1} following potentiostatic polarization for 3600 s. Additionally, the t-AgPdIr catalyst shows an enhanced turnover frequency value of 407.3 h^{-1}, a higher volume of generated H_2 gas up to 51.8 mL after 120 min of reaction, and an activity recovery of 90.7% after five reaction cycles. Impressively, compared with the as-prepared nanoalloy, the postreaction catalyst shows a stable strain state along the twin boundaries and a surface segregation of Pd and Ir elements after the formate oxidation and dehydrogenation reactions.

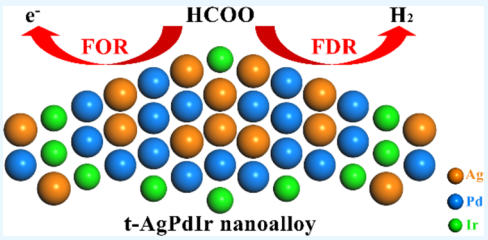

INTRODUCTION

Hydrogen has attracted an increasing level of attention as an important energy vector due to its high energy density, cleanliness, and renewability.[1] Large-scale gaseous hydrogen storage that is both safe and effective is still a pressing issue that has to be resolved.[2] Creating a technique to liberate ultrapure hydrogen from solid salts has surfaced as a possible means of improving the fuel's handling and transportation characteristics.[3] Formate, when compared to H_2O molecules as hydrogen carriers in water electrolysis, exhibits several advantages.[4] First, it can potentially carry a greater amount of hydrogen. Second, it is more flexible and easily integrates with current transportation infrastructures. Lastly, it can carry hydrogen at low pressure and temperatures close to ambient.[5] For these reasons, formate is a promising option for hydrogen carriers, as well as direct formate fuel cells. The former can be used to generate hydrogen in situ and supply high-purity hydrogen to a proton exchange membrane fuel cell when needed.[6,7] The practical uses of future cell technology are hampered by the slow reaction kinetics of the formate oxidation and dehydrogenation reactions involved.[8]

Several attempts have been undertaken to enhance the formate oxidation and dehydrogenation reaction-related catalytic characteristics of Pd-based catalysts.[9,10] In order to improve the catalytic capabilities of the FOR, for instance, our previous study created an inverted AgPdF nanoalloy with a robust interface structure. Moreover, the presence of more high-valence Ag sites on the active surface can bolster OH adsorption and OH-radical desorption.[11] The O-functional groups are essential for lowering the activation energy, according to Dong et al.'s investigation into the kinetics of surface-functionalized Pd on carbon catalysts for the formate dehydrogenation process (FDR).[7] Through the interconversion of widely accessible (bi)carbonate and formate salts under very moderate reaction conditions, Wei et al. established a feasible technique for Mn-promoted hydrogen storage and release. The optimized dehydrogenation step has significantly enhanced the hydrogen storage-release efficiency.[12] As a very effective FDR catalyst, Pan et al. produced a PdAu nanoalloy supported on nickel foam. The special nanodendritic structure supplied more active sites to encourage the dehydrogenation of formate.[13] However, in order to customize the adsorption characteristics of the active site and subsequently affect the catalytic activity of the Pd-based nanoalloys, the synergistic adjustment of the physicochemical features of intrinsic active surface is essential.[14]

Recently, the integration of mirror-symmetrical crystal planes can offer the twinned structure with high-energy twin boundaries that are frequently found in nanomaterials.[15] The

Received: April 15, 2024
Revised: October 17, 2024
Accepted: October 28, 2024
Published: November 5, 2024

https://doi.org/10.1021/acsomega.4c03637
ACS Omega 2024, 9, 45811−45821

metastable Pd nanoparticles with twin borders were synthesized by Liu et al. in order to minimize poisoned active sites and speed up the catalytic process.[16] The rising twin boundaries in Pd catalyst were developed by Huang et al., and the twinned structure with strain can reduce the barriers to activation and desorption.[17] By creating unique Pd2CoAg nanocrystals with twinned surfaces, Liu et al. were able to adjust the binding of H or O atoms to increase catalytic activity.[18] The abundant active sites along the twin boundaries can be produced by the twinned structures in nanoparticles, and the strain effect can further modify the catalytic characteristics of the active site by structural disturbance close to the twin boundary.[19]

It has been established that surface reconstruction occurs in Pd-based nanoalloys during catalysis.[20,21] There is ample evidence that during catalysis, the surface sites of nanoalloys may not remain in their prepared state and that the postreaction catalysts will change in composition and structure as a result of the reaction conditions.[22] Tao et al. presented the restructuring behavior of Rh−Pd core−shell structured bimetallic catalyst under the reaction conditions, and the surface region of the as-prepared RhPd nanoalloy restructured to Pd-rich surface in the reducing atmosphere.[23] Jiang et al. discussed the surface restructuring of the ternary Pd−Pt−Cu nanocatalysts under the formic acid oxidation, and the Pt/Pd agglomeration and partial Cu dealloying were observed after the repeated potential cycling.[24] The physicochemical characteristics of real catalytically active sites cannot be reflected in the composition and structure of the nanoalloy as it has been manufactured, which could potentially cause errors in the logical design of future catalysts. Conversely, examining the evolution of reconstruction in the postreaction catalyst could aid in the development of a trustworthy structure−property correlation in the Pd-based nanoalloy.

In this study, we present the improved catalytic characteristics of the single-twinned AgPdIr (t-AgPdIr) nanoalloy for the formate oxidation and dehydrogenation reactions. The t-AgPdIr nanoalloy displayed a downshift of the d-band center and a distribution of compressive and tensile strains along the twin boundary when compared to the AgPd nanoalloy. The t-AgPd catalyst demonstrated a greater peak current density, reduced onset potential, and activity retention for the FOR while retaining its strain distribution along the twin boundary. Furthermore, the t-AgPdIr catalyst with the stable twinned structure showed improved activity recovery, turnover frequency value, and volume of generated H_2 gas, indicating improved catalytic performance for hydrogen generation. More significantly, the postreaction t-AgPdIr catalyst exhibits the surface segregation of Pd and Ir elements following the catalytic processes, in contrast to the nanoalloy as synthesized. To the best of our knowledge, this study is the first report of the surface reconstruction of a single-twinned AgPdIr nanoalloy with bifunctional catalytic properties during formate oxidation and dehydrogenation reactions.

EXPERIMENTAL SECTION

Synthesis Methods. *Single-Twinned AgPdIr (t-AgPdIr) Nanoalloy.* In a typical synthesis of t-AgPdIr nanoalloy, 2 mM $AgNO_3$ and 2 mM $Pd(acac)_2$ were added in 10 mL of 1-octadecene solution. After continuous stirring, 6 mL of oleylamine was introduced into the above solution, and then the reactor was heated to 523 K for 5 min. Subsequently, 2 mM $IrCl_4$ solution was rapidly injected into the mixture, and the constant temperature reaction was maintained for 25 min. The product was collected by centrifugation and washed 3 times with ethanol after cooling to room temperature. The as-obtained nanoalloy was treated with 1,2-ethylenediamine at 333 K for 12 h and then washed with ethanol and deionized water twice. The final product was freeze-dried overnight.

AgPd Nanoalloy. AgPd nanoalloy was also synthesized using a method similar to that for the t-AgPdIr nanoalloy. In this case, only $AgNO_3$ and $Pd(acac)_2$ were employed as the metal precursors.

Physical Characterization. Using transmission electron microscopy (TEM) and high-resolution TEM (HRTEM, FEI Tecnai F30), we obtained the precise morphology and nanostructure of the catalysts were obtained. Energy-dispersive X-ray (EDX) spectroscopy was used to perform compositional studies. By using a plugin script that was placed in GATAN Digital Micrograph Software, geometric phase analysis (GPA) and fast Fourier transform (FFT) patterns were made possible. To reduce the fluctuations, digital processing with a high spatial resolution (5 nm) was used, the observed strain's standard deviation for this spatial resolution is 0.1−0.2%. A particular crystal plane direction is denoted by e_{xx} in the strain analysis, and its vertical direction is denoted by e_{yy}.[25] Using PANalytical X'Pert Pro MPD equipment equipped with Cu Kα radiation, X-ray diffraction (XRD) was used to determine the phase and crystallinity of the samples. Characterization by X-ray photoelectron spectroscopy (XPS) was done with the Kratos (Axis Supra) instrument with Al (Ka = 1486.6 eV). The formula, $\int N(\varepsilon)\varepsilon d\varepsilon / \int N(\varepsilon) d\varepsilon$, between 0 and 12 eV binding energy was used to establish the d-band center locations. $N(\varepsilon)$ stands for the density of states, and the Shirley background was removed from the obtained XPS spectra.

Catalytic Testing. A typical three-electrode system and a CHI 660C electrochemical workstation (Shanghai Chenhua, China) were used in the setup for all electrochemical experiments, which were carried out at room temperature. Prior to surface coating, the glassy carbon electrode (GCE), which served as the working electrode, was polished in steps using an alumina slurry at 0.3, 0.05, 1, and 0.5 μm. The as-synthesized catalysts were ultrasonically dispersed in alcohol and Nafion mixing solution to generate the catalyst ink, which was then used to prepare a catalyst-modified GCE. Next, 5 μL of the dispersion was applied on the GCE's surface and was allowed to dry naturally. As the working electrode, counter electrode, and reference electrode for the FOR, respectively, the catalyst-modified GCE, Pt electrode, and mercury−mercury oxide (Hg/HgO) were used.

All electrochemical experiments were performed in a setup consisting of a CHI 660C electrochemical workstation (Shanghai Chenhua, China) and a standard three-electrode system at room temperature. The glassy carbon electrode (GCE) as the working electrode was successively polished with alumina slurry (1, 0.3, and 0.05 μm) before the surface coating. For preparing a catalyst-modified GCE, the as-synthesized catalysts were dispersed ultrasonically in alcohol and Nafion mixing solution to form the catalyst ink. Afterward, 5 μL of the dispersion was deposited onto the surface of the GCE and dried naturally. For the FOR, the catalyst-modified GCE, Pt electrode, and mercury−mercury oxide (Hg/HgO) were deployed as the working electrode, counter electrode, and reference electrode, respectively. Unless otherwise noted, all potential values in this paper were referenced to the RHE.

https://doi.org/10.1021/acsomega.4c03637
ACS Omega 2024, 9, 45811−45821

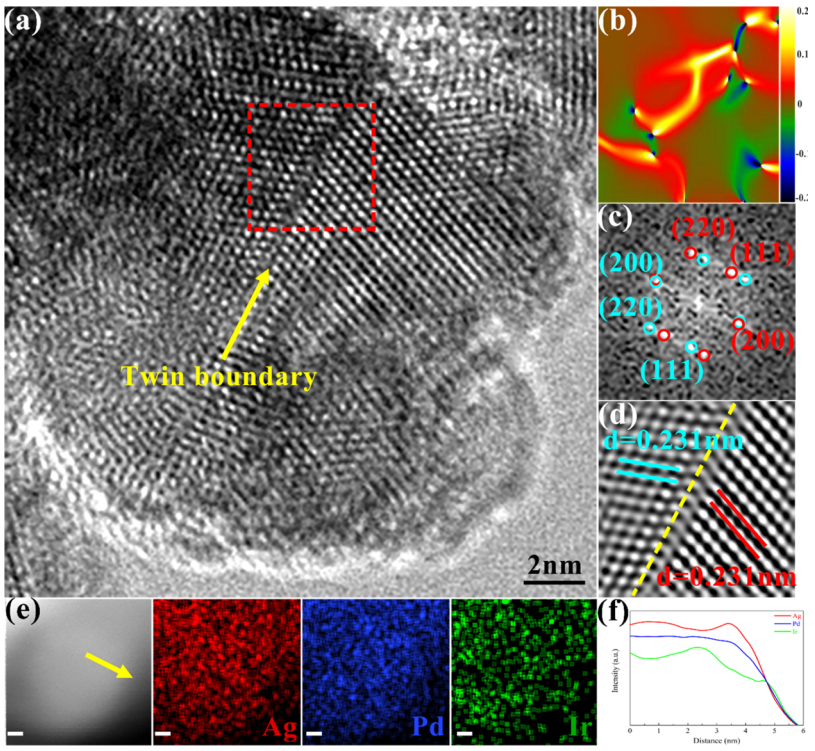

Figure 1. (a) HRTEM image of the single-twinned AgPdIr (t-AgPdIr) nanoalloy. (b) Strain distribution of the e_{yy} direction for the typical nanoparticle. The distribution of blue and red regions exhibits the compressive and tensile strains in the t-AgPdIr nanoalloy. (c) FFT and (d) IFFT patterns of the corresponding region of the twin boundary structure in HRTEM image. (e) HAADF-STEM and EDX elemental mapping images of the AgPd nanoalloy. (f) EDX line profiles extracted from the typical lines in HAADF-STEM image.

Research-grade gases were used for all electrochemical tests, which were conducted at room temperature.

Cyclic voltammetry (CV) was used to measure the catalytic activity of a N_2-saturated 1 M KOH solution and 1 M KOH mixed with 1 M HCOOK solution, respectively, at a sweep rate of 50 mV·s^{-1}. Catalytic activity is calculated using the current densities of the anodic peaks in the forward direction. Chronoamperometry (CA) measurements were used to examine the stability of the catalytic process in a solution of 1 M HCOOK mixed with N_2-saturated 1 M KOH. Assuming a value of 405 μC·cm^{-2} for the adsorption of an oxygen monolayer, the charge in the Pd oxidation peak region was integrated to determine the electrochemically active surface areas (ECSA) of the catalysts.

100 mL glass reactors were used for the hydrogen-generating trials. The gas outlet was linked to a gas buret after being coupled to NaOH and CuCl solution traps. The CO_2 and CO produced by the reactor were absorbed using the 2 M NaOH and 2 M CuCl solution. The combination of 10 mg of catalysts in 6 M HCOOK solution was stirred to start the catalytic hydrogen production process. After the hydrogen production trials, the catalysts were centrifuged from the formate solution, cleaned three times with deionized water, and freeze-dried for the stability test. The following reaction cycle then used the recovered catalyst. The scale difference on the gas buret was recorded in order to determine the quantities of hydrogen production.

RESULTS AND DISCUSSION

The single-twinned AgPdIr (t-AgPdIr) nanoalloy's micromorphology, strain, and composition analysis are displayed in Figure 1, and Figures S1 and S2 display the SEM and low-magnification TEM images of the as-synthesized t-AgPdIr nanoalloy. A single 15 nm nanoparticle is shown in the field of view in the HRTEM image. Remarkably, at the junction of the mirror-symmetric extension directions and the lattice fringes, a twin boundary is seen. Figure 1b shows an additional strain distribution picture of a single nanoparticle. The coexistence of compressive and tensile stresses in the e_{yy} direction of the t-AgPdIr nanoalloy is evident from the alternating distributions of the red and dark blue areas. The blue and dark red areas are situated close to the nanoparticle's double border. The twin border can either directly increase catalytic activity by acting as active sites or indirectly through the strain effect caused by structural instabilities at the twin boundary, similar to the reported metastable Pd with numerous twin boundaries.[16] Two sets of bright spots are shown by red and cyan circles, respectively, in the FFT pattern of the same region in the HRTEM picture, which is shown in Figure 1c. Four pairs of the diffraction spot associated with the typical crystal planes (111) and (220) are offset from one another by a symmetric distribution when combined with the HRTEM image. Additionally, the diffraction spots from two distinct sets meet to form a pair that are part of the twin boundary's crystal plane information, which is the (200) characteristic crystal plane. The twin boundary at the borders of the lattice fringes extending in different directions is also highlighted in Figure 1d, which shows the IFFT pattern that corresponds to the FFT pattern. The lattice fringe interplanar spacing for the (111) crystal plane in the twin boundary region of the t-AgPdIr nanoalloy is 0.231 nm. Figure 1e displays the High-angle annular dark-field imaging-scanning TEM (HAADF-STEM) image and EDX elemental mapping of the t-AgPdIr nanoalloy, which reveal that every element is equally distributed

https://doi.org/10.1021/acsomega.4c03637
ACS Omega 2024, 9, 45811−45821

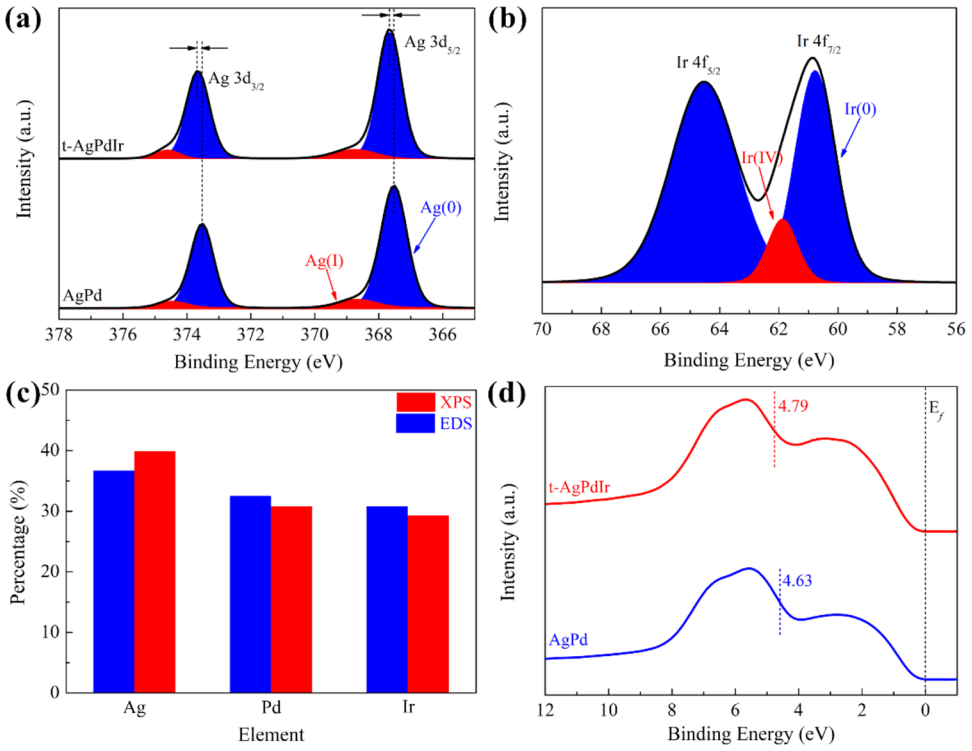

Figure 2. High-resolution XPS spectrum of (a) Ag 3d and (b) Ir 4f in the t-AgPdIr and AgPd nanoalloys. (c) Atomic percentage of Ag, Pd, and Ir for the as-prepared t-AgPdIr nanoalloy based on the XPS and EDS analysis. (d) Surface VBS for the t-AgPdIr and AgPd nanoalloys; the dashed lines indicate the positions of the d-band center with respect to the Fermi level.

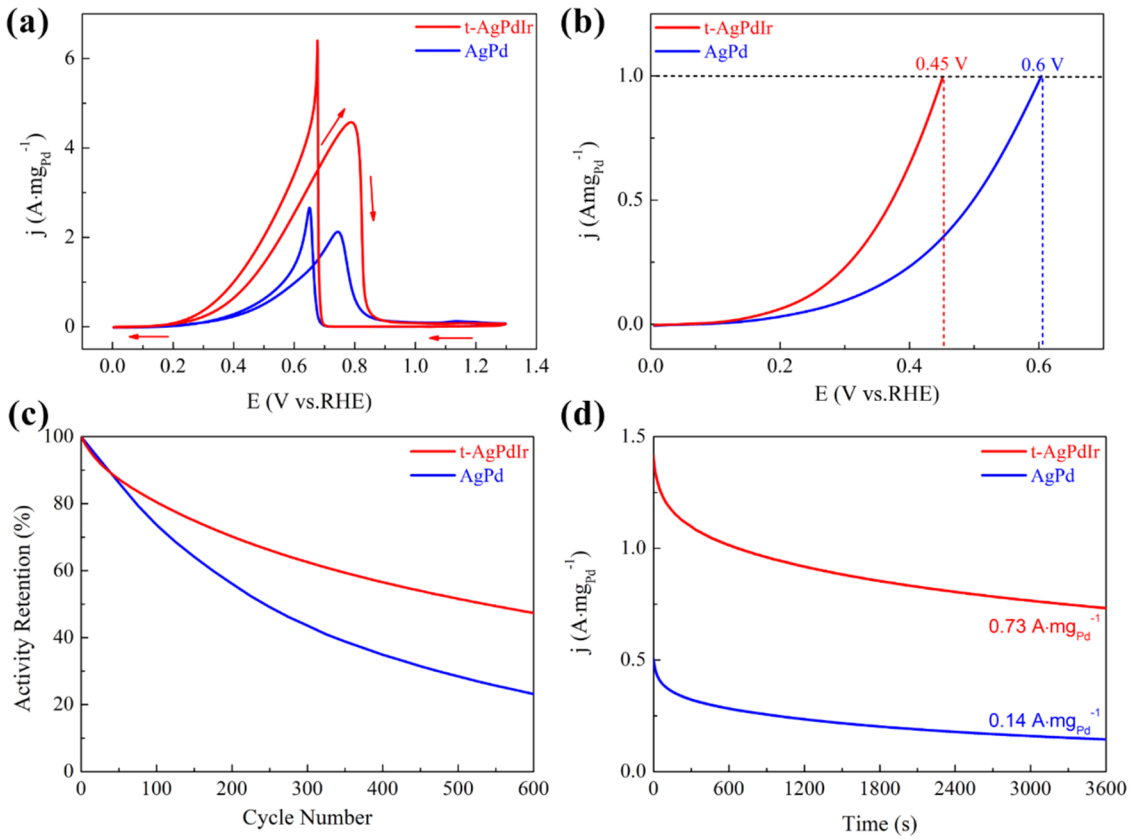

Figure 3. (a) CV curves of the formate oxidation reaction for the t-AgPdIr catalyst compared with that for the AgPd catalyst. (b) Enlarged CV curves only in positive direction from (a). (c) Activity retentions within 600 CV cycles of t-AgPdIr and AgPd catalysts. (d) CA curves at 0.4 V of the t-AgPdIr and AgPd catalysts for 3600 s.

https://doi.org/10.1021/acsomega.4c03637
ACS Omega 2024, 9, 45811−45821

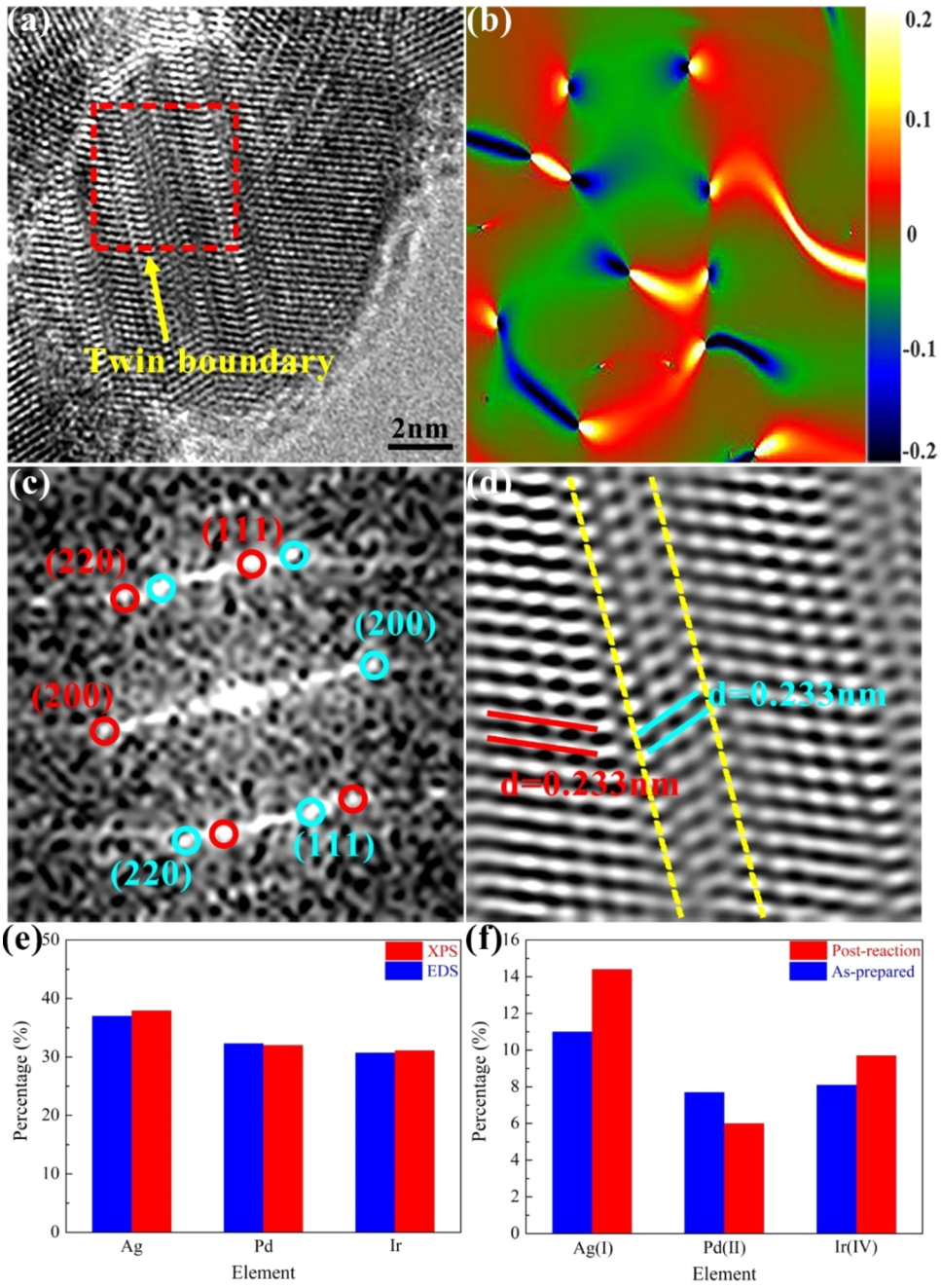

Figure 4. T-AgPdIr catalyst after formate oxidation reaction: (a) HRTEM image, (b) strain distribution, (c) FFT and (d) IFFT patterns of the corresponding region in HRTEM image, (e) atomic percentages of Ag, Pd, and Ir based on the XPS and EDS analysis, and (f) percentages of Ag(I), Pd(II), and Ir(IV) calculated from fitted XPS spectra in postreaction catalyst compared with that in the as-prepared nanoalloy.

throughout the nanoparticle. Figure 1f displays the EDX line profile that was derived from the typical line in the HAADF-STEM picture. It demonstrates how equally distributed the elements Ag, Pd, and Ir are within the nanoparticle. In addition, Figure S3 shows the micromorphology and strain analysis of the AgPd nanoalloy, whose low-magnification TEM picture is shown in Figure S1a. The strain distribution image of a single nanoparticle is displayed, and the lattice fringes are clearly visible in a typical nanoparticle with a particle size of around 17 nm. The FFT and inverse FFT (IFFT) patterns of the same location in the HRTEM picture show lattice fringes with an interplanar spacing of 0.228 nm for the (111) typical crystal plane. Figure S4 displays the XRD patterns of the AgPd and t-AgPdIr nanoalloys. The diffraction peaks of the AgPdIr nanoalloy are similar to those of the AgPd nanoalloy, indicating that the alloying-related crystal structure is stable overall. Furthermore, the XRD pattern's rise in 2θ may signify the ternary alloying structure creation of AgPdIr following the inclusion of the Ir element.

Figure 2 compares the surface compositions of the t-AgPdIr and AgPd nanoalloys. After calibration with C 1s at 284.8 eV, strong peaks for each included element are apparent. The XPS survey spectra of the AgPd and t-AgPdIr nanoalloys as produced are displayed in Figure S5a. Apart from the same spectra peaks of Ag and Pd elements, the AgPdIr nanoalloy displays a distinct Ir element spectra peak, as seen in the picture. Figure 2a,b, respectively, displays the high-resolution XPS spectra of the AgPd and t-AgPdIr nanoalloys. The binding

https://doi.org/10.1021/acsomega.4c03637
ACS Omega 2024, 9, 45811−45821

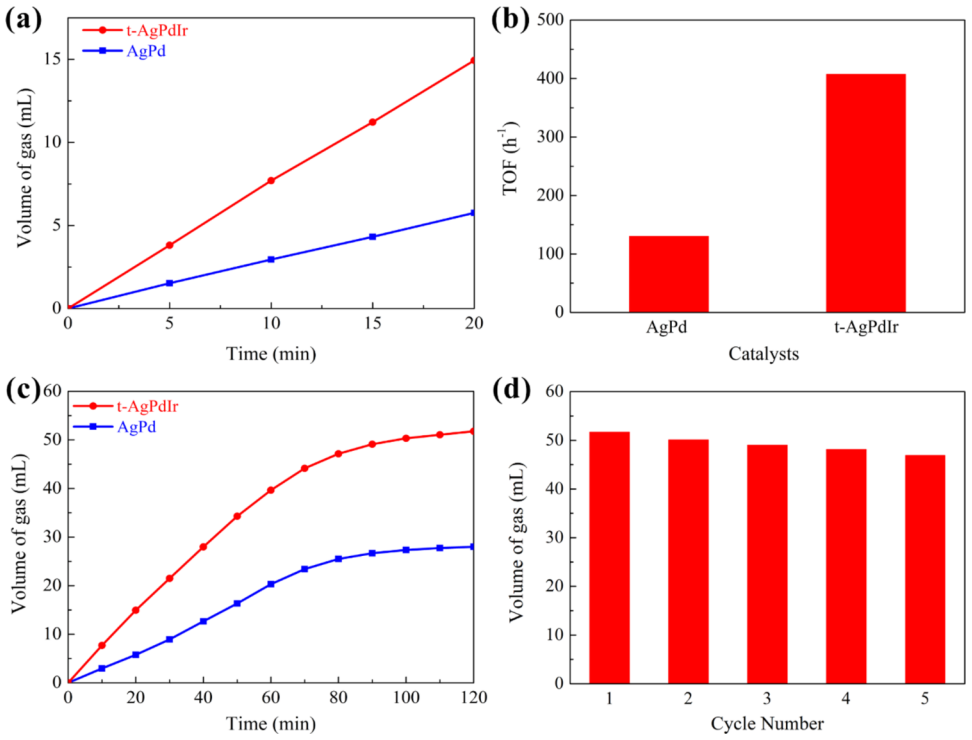

Figure 5. Catalytic performance of hydrogen generation for the t-AgPdIr and AgPd catalysts. (a) Volume of generated H_2 gas versus reaction time of 20 min and (b) the corresponding TOF values for the t-AgPdIr catalyst compared with that of the AgPd catalyst. (c) Volume of generated H_2 gas versus reaction time of 120 min for the t-AgPdIr catalyst compared with that of the AgPd catalyst. (d) Volume of generated H_2 gas for 120 min in various cycles of the t-AgPdIr catalyst.

energies of Ag $3d_{5/2}$ peak in the t-AgPdIr nanoalloy are positively displaced to 367.7 eV when compared to the AgPd nanoalloy and negatively shifted to 334.5 eV when compared to the AgPd nanoalloy. A similar pattern can be seen when comparing the Ag $3d_{3/2}$ and Pd $3d_{3/2}$ peaks in the high-resolution XPS spectra of the two nanoalloys. Tables S1 and S2 list the Ag and Pd surface compositions and XPS spectral peak locations in the various nanoalloys. Figure 2d shows the Ir 4f high-resolution XPS spectra of the t-AgPdIr nanoalloy. The Ir $4f_{7/2}$ and Ir $4f_{5/2}$ peaks of the Ir (0) component are located at binding energies of 60.9 and 64.8 eV, whereas the strong peak of the Ir(IV) component is at 61.9 eV. The EDS and XPS results of Figure 2c show that the Ag, Pd, and Ir bulk and surface compositions in the t-AgPdIr nanoalloy are distinct. The atomic percentage of Ag element is 36.7% in the as-prepared t-AgPdIr nanoalloy based on the EDS analysis, while that based on the XPS analysis increases to 39.9% in as-prepared nanoalloy, indicating that Ag atoms are preferentially enriched on the surface of the nanoparticles. Moreover, the XPS valence band spectra (VBS) of the AgPd and t-AgPdIr nanoalloys are displayed in Figure 2d. The t-AgPdIr nanoalloy's d-band center is at −4.79 eV, which is a negative shift from the AgPd nanoalloy's location of −4.63 eV. One frequent explanation for the d-band center downshift of t-AgPdIr nanoalloy is electron transport.[26]

Figure 3 compares the catalytic performance of AgPd and t-AgPdIr catalysts for the formate oxidation reaction (FOR). Figure 3a displays the CV curves of the AgPd and t-AgPdIr catalysts, with red arrows showing in the scan's direction. The AgPd catalyst has a value of 4.6 A·mg_{Pd}^{-1} for the oxidation peak current density, but the t-AgPdIr catalyst has a value 1.2 times higher. The early potential range of 0−0.6 V is shown by the only positive CV curves in Figure 3b, which were created from Figure 3a. The t-AgPdIr catalyst outperforms the AgPd catalyst at 0.6 V, showing the lowest onset potential of 0.45 V. Figure 3c shows the activity retentions of t-AgPdIr and AgPd catalysts during 600 cycles of cyclic voltammetry, whereas Figure S6 shows the CV curves for these catalysts' initial, 300th, and 600th cycles. AgPd catalyst demonstrates only a comparable activity retention for the first 100 cycles before sharply falling to a final activity retention of just 22.6% in the subsequent cycles. In contrast, the t-AgPdIr catalyst exhibits an activity retention of 47.6%. Table S3, which presents the catalytic properties of the t-AgPdIr catalyst and previous FOR catalysts, shows that the t-AgPdIr catalyst has the greatest current density of catalytic activity among the published FOR catalysts. Especially compared with the conventional AgPdIr nanoalloy,[10] the t-AgPdIr nanoalloy exhibits a 4.24 times higher specific activity and a 1.05 times higher mass activity. Based on the above comparison results, the influence of the twinning structure in the t-AgPdIr nanoalloy on catalytic activity is more appropriately demonstrated. Significant information about the catalytic stability of t-AgPdIr and AgPd catalysts may be gleaned from the CA curves in Figure 3d. Compared to the AgPd catalyst, which experiences a sharp decline in current density over time, the t-AgPdIr catalyst exhibits a higher current density. But after the CA test, the t-AgPdIr catalyst keeps a current density of 0.73 A·mg_{Pd}^{-1}, which is 5.2 times higher than the AgPd catalyst.

Following the FOR, more research is done on the composition and structural details of the nanoalloys in order to better understand the relationship between the dynamic reconstruction under the working conditions and the catalytic stability of t-AgPdIr catalysts. The micromorphology, strain,

https://doi.org/10.1021/acsomega.4c03637
ACS Omega 2024, 9, 45811−45821

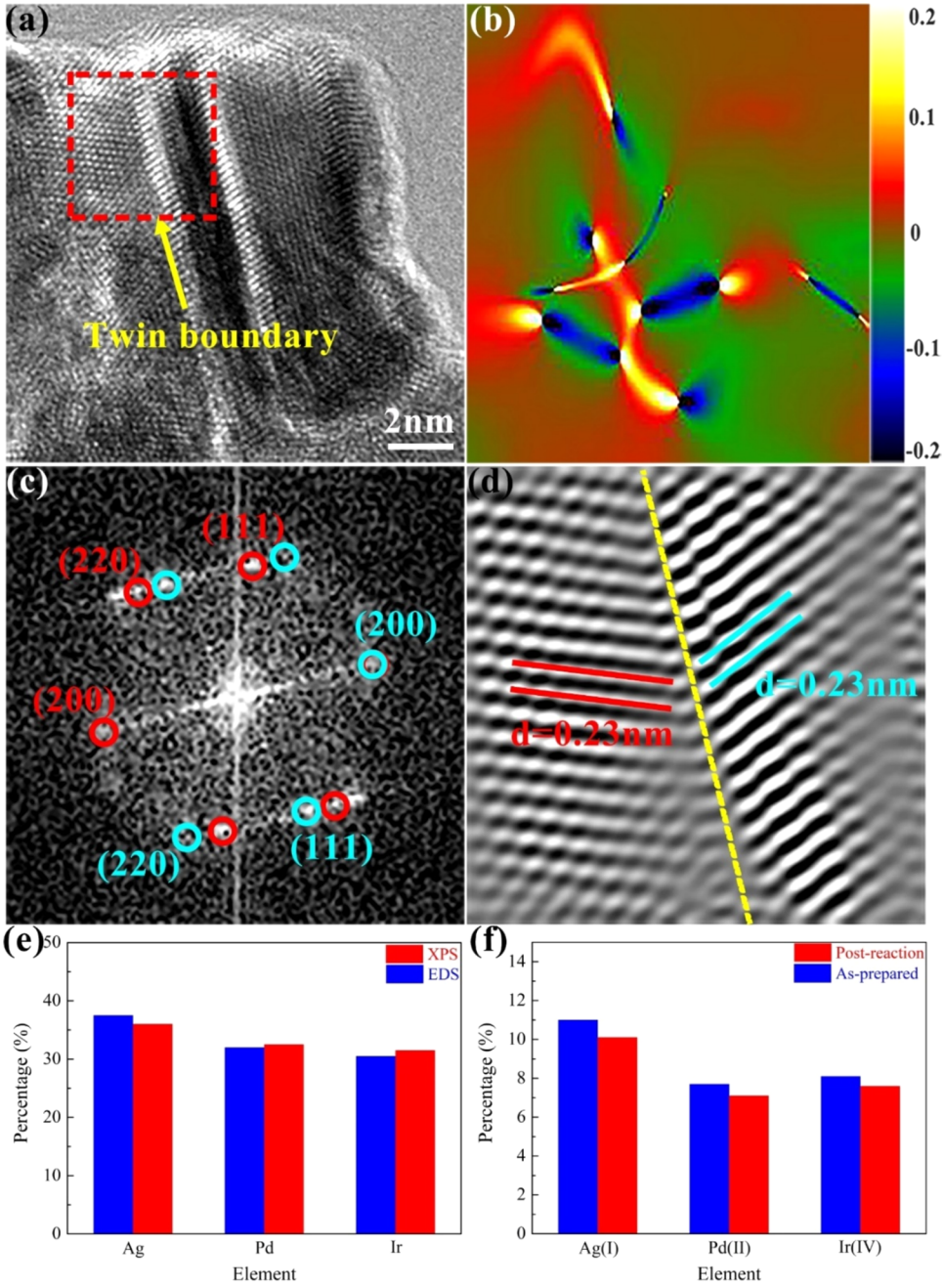

Figure 6. T-AgPdIr catalyst after formate dehydrogenation reaction: (a) HRTEM image, (b) strain distribution, (c) FFT and (d) IFFT patterns of the corresponding region in HRTEM image, (e) atomic percentages of Ag, Pd, and Ir based on the XPS and EDS analysis, and (f) percentages of Ag(I), Pd(II), and Ir(IV) calculated from fitted XPS spectra in postreaction catalyst compared with that in the as-prepared nanoalloy.

and composition characterization of the t-AgPdIr catalyst following FOR are displayed in Figure 4. A typical 12 nm-sized nanoparticle's HRTEM picture is shown in Figure 4a, where several twin borders are visible. The strain distribution picture in Figure 4b shows that tensile and compressive stresses are localized at the twin boundary, especially in the red and blue areas. This implies that after the FOR, the stresses are more pronounced in the t-AgPdIr catalyst. Two sets of brilliant spots, highlighted in red and cyan, correspond to lattice fringes of the (111) crystal plane with an interplanar spacing of 0.233 nm in the twin border area, according to the matching FFT and IFFT patterns in Figure 4c,d. The HAADF-STEM image's line profile and the EDX elemental mapping in Figure S7b,c demonstrate how evenly distributed the Ag, Pd, and Ir contents are within the nanoparticle. Figure S8 displays the high-resolution XPS spectra of Ag 3d, Pd 3d, and Ir 4f in the postreaction t-AgPdIr catalyst and compares them to the spectra in the synthesized t-AgPdIr nanoalloy. The EDS and XPS composition data for the postreaction t-AgPdIr catalyst after the FOR are shown in Figure 4e. Based on the XPS examination, the percentages of Pd and Ag components rise to 32 and 31.1%, respectively, as compared to the nanoalloy as manufactured. The percentages of various compounds determined from fitted XPS spectra in the postreaction catalyst are further presented in Figure 4f in comparison to the as-prepared nanoalloy. Ag(I), Pd(II), and Ir(IV) make up 11, 7.7, and 8.1% of the as-prepared t-AgPdIr nanoalloy, respectively.

https://doi.org/10.1021/acsomega.4c03637
ACS Omega 2024, 9, 45811−45821

Table 1. EDS, XPS Composition, and the Content of High-Valence Metal in the As-Prepared and Postreaction t-AgPdIr Catalysts

				postreaction t-AgPdIr					
catalysts	as-prepared t-AgPdIr			after the FOR			after the FDR		
EDS	Ag	Pd	Ir	Ag	Pd	Ir	Ag	Pd	Ir
	36.7%	32.5%	30.8%	37%	32.3%	30.7%	37.5	32%	30.5%
XPS	Ag	Pd	Ir	Ag	Pd	Ir	Ag	Pd	Ir
	39.9%	30.8%	29.3%	37.9%	32%	31.1%	36%	32.5%	31.5%
content	Ag(I)	Pd(II)	Ir(IV)	Ag(I)	Pd(II)	Ir(IV)	Ag(I)	Pd(II)	Ir(IV)
	11%	7.7%	8.1%	14.4%	6%	9.7%	10.1%	7.1%	7.6%

Ag(I) and Ir(IV) percentages in the postreaction catalyst rise to 14.4 and 9.7%, respectively, following the FOR.

Figure 5 compares the catalytic performance of t-AgPdIr and AgPd catalysts for the generation of hydrogen. Figure 5a displays the amount of hydrogen generated and the reaction time curves for both catalysts during the first 20 min of the process. The nearly straight lines show how active each catalyst is at producing hydrogen. The AgPd catalyst produces 5.8 mL of H_2 gas after 20 min, whereas the t-AgPdIr catalyst produces 14.9 mL of H_2 gas, which is 1.7 times greater. In Figure 5b, the AgPd catalyst and the t-AgPdIr catalyst's formate dehydrogenation reaction (FDR) turnover frequency (TOF) are compared. The results show that the AgPd catalyst has a TOF value of 407.3 h^{-1}, 3.1 times that of the t-AgPdIr catalyst. Figure 5c shows the volume of H_2 gas produced by the aforementioned catalysts during a prolonged hydrogen production reaction. The generated H_2 gas volume by the AgPdIr catalyst reaches 51.8 mL at the end of the 120 min reaction. The catalytic characteristics of the t-AgPdIr catalyst and earlier FDR catalysts are given in Table S4, which demonstrate that the t-AgPdIr catalyst presents the highest TOF and generated H_2 volume among the published FDR catalysts. Compared with our previous work for the single-twinned AgPdF catalyst,[27] the significant increase in hydrogen production of the t-AgPdIr nanoalloy within the same time can be attributed to the introduction of Ir element, and the formation of this ApPdIr ternary alloy structure can effectively modulate the surface electronic structure of the nanoparticles.[10] Figure S9 displays the volume of H_2 gas generated by the t-AgPdIr catalyst at different concentrations of Ir source in the precursor. The results show that while the volume of H_2 gas generated by the catalyst actually decreases as Ir source concentrations increase from 2 to 4 mM, it increases significantly when Ir source concentrations increase from 1 to 2 mM. Further kinetic information on the FDR in Figure S10 is obtained by examining the effects of reaction temperature and formate concentration. It is clear that the volume of H_2 gas produced by the t-AgPdIr catalyst progressively increases as the formate concentration rises. As the concentration rises from 6 to 8 M, the t-AgPdIr catalyst's TOF value actually falls. Furthermore, the TOF of FDR of the t-AgPdIr catalyst increases proportionately with an increase in the reaction temperature. The volume of H_2 gas produced by the AgPdIr catalyst cannot rise any higher once the reaction temperature reaches 333 K. Figure S11 shows the volume of generated H_2 gas of the t-AgPdIr catalyst in different reaction solutions, which indicates that the volume of generated H_2 gas of the t-AgPdIr catalyst significantly reduces with the introduction of formic acid, while the different formate species as reaction solutions have no impact on the catalytic performance of the t-AgPdIr catalyst. The catalytic stability of the FDR for the t-AgPdIr catalyst is displayed in Figure 5d. Following the second, third, fourth, and fifth gas production reactions, the recycled catalyst produced 50.2, 49.1, 48.2, and 47 mL of H_2 gas, respectively. The newly created catalyst produced 51.8 mL of H_2 gas. The volume of generated H_2 gas after the fifth reaction run is still 90.7% of its initial activity; compared with the initial reaction, the catalytic performance of the t-AgPdIr catalyst is only slightly reduced after five reaction cycles.

More notably, Figure 6 (right) displays the micromorphology, strain, and composition characterization of the t-AgPdIr catalyst following the FDR. The HRTEM image of the t-AgPdIr catalyst following the FDR is shown in Figure 6a, displaying a stable twinned structure in a 13-nm-sized nanoparticle. Both the black and red zones are maintained along the twin border, as can be seen in the strain distribution picture shown in Figure 6b. According to this, the remaining compressive and tensile stresses at the twin border after the FDR are stabilized by the t-AgPdIr catalyst. The lattice fringes of the (111) crystal plane are shown by two sets of brilliant spots, each ringed in red and cyan, respectively, with an interplanar spacing of 0.23 nm. In Figure 6c,d, the relevant FFT and IFFT patterns are displayed. The twin boundary between two lattice fringe areas with distinct extending orientations is also seen in the IFFT pattern. From the EDX elemental mapping and the line profile of the HAADF-STEM picture in Figure S12b,c, three elements are evenly distributed in the t-AgPdIr catalyst after FDR. The high-resolution XPS spectra of Ag 3d, Pd 3d, and Ir 4f in the postreaction t-AgPdIr catalyst following the FDR are presented in Figure S13, along with a comparison with the as-prepared t-AgPdIr nanoalloy. Figure 6e displays the composition of the postreaction t-AgPdIr catalyst as determined by XPS and EDS analysis following the FDR. The percentages of Pd and Ag components based on the XPS examination further increase to 32.5 and 31.5%, respectively, as compared to the nanoalloy as-prepared. The percentages of various compounds determined from fitted XPS spectra in the postreaction catalyst are further presented in Figure 4f in comparison to the as-prepared nanoalloy. Ag(I), Pd(II), and Ir(IV) percentages in the postreaction catalyst decreased marginally to 10.1, 7.1, and 7.6% in comparison to the nanoalloy as made.

Table 1 provides the high-valence metal content, EDS, and XPS composition of the as-prepared and postreaction t-AgPdIr catalysts. According to the EDS data, the t-AgPdIr catalysts' overall composition is almost entirely constant both before and after the reaction, with very little variation in composition. More importantly, the XPS results show that the surface Ag content of the as-prepared t-AgPdIr catalyst is significantly higher than the overall composition content obtained from EDS results, and the surface segregation of Ag element can be

https://doi.org/10.1021/acsomega.4c03637
ACS Omega 2024, 9, 45811−45821

owing to lower surface energy under the vacuum[28] and low intermediate coverage.[29] Following the FOR, the surface Pd content of the postreaction t-AgPdIr catalysts increases significantly relative to the as-prepared condition. Additionally, an increase in the surface Ir(IV) content may cause an increase in the surface Ir content of the postreaction t-AgPdIr catalyst. Additionally, following the FDR, the t-AgPdIr catalyst's surface content of Pd and Ir increased similarly. During the catalytic reaction process, the adsorption of reactants, intermediates, and products by Pd and Ir induces atomic segregation from the subsurface to the surface, resulting in the formation of a preferred structure with low surface energy.[10,21,30] AgPdIr nanoalloys' ability to form more surface active sites, which are essential for the adsorption and activation steps in catalytic reactions, is greatly impacted by the above surface reconstruction behavior.[10,18,31] In addition, surface reconstruction can alter the surface chemical environment of catalysts, affecting the interactions between reactants and catalysts.[32]

CONCLUSIONS

To sum up, the AgPdIr nanoalloy that is single-twinned (t-AgPdIr) exhibits better catalytic activity and stability when it comes to formate oxidation and dehydrogenation reactions. The t-AgPdIr nanoalloy exhibits a downshift of the d-band center and a dispersion of compressive and tensile strains along the twin boundary when compared to AgPd nanoalloy. A lower onset potential of 0.45 V, a greater activity retention of 47.6% after 600 cycles, a higher peak current density of 4.6 $A{\cdot}mg_{Pd}^{-1}$, and a higher current density of 0.73 $A{\cdot}mg_{Pd}^{-1}$ following the potentiostatic polarization for 3600 s are all demonstrated by the t-AgPdIr catalyst. The catalyst known as t-AgPdIr exhibits enhanced catalytic performance of hydrogen generation, as evidenced by its higher turnover frequency value of 407.3 h^{-1}, greater volume of generated H_2 gas up to 51.8 mL after 120 min of reaction, and an activity recovery of 90.7% after five reaction cycles. In addition, the t-AgPdIr nanoalloys exhibit a surface segregation of Pd and Ir elements following the formate oxidation and dehydrogenation reactions, as well as a stable strain distribution at the twin boundaries. According to these results, the twinned structure that AgPdIr catalysts can produce and maintain a stable strain state throughout catalysis, and segregation structures offer better bifunctional catalytic characteristics for the reactions of formate oxidation and dehydrogenation.

ASSOCIATED CONTENT

Supporting Information

The Supporting Information is available free of charge at https://pubs.acs.org/doi/10.1021/acsomega.4c03637.

XPS surface composition analysis in the t-AgPdIr and AgPd nanoalloys (Tables S1 and S2); literature survey of the catalytic activity of FOR and FDR catalysts (Tables S3 and S4); SEM and TEM image of t-AgPdIr and AgPd nanoalloys (Figures S1−S3); XRD and XPS pattern of t-AgPdIr and AgPd nanoalloys (Figures S4 and S5); CV curves in 1st, 300th, and 600th cycles of t-AgPdIr and AgPd catalysts (Figure S6); EDX and XPS analysis of the t-AgPdIr catalyst after FOR (Figures S7 and S8); volume of generated H_2 gas for the t-AgPdIr catalyst with changes in catalyst composition, reaction solution concentration, reaction solution temperature, and reaction solution composition (Figures S9−S11); EDX and XPS analysis of the t-AgPdIr catalyst after FDR (Figures S12 and S13), and XRD patterns of the t-AgPdIr nanoalloys after the FOR and FDR (Figure S14) (PDF)

AUTHOR INFORMATION

Corresponding Author

Fuyi Chen − *State Key Laboratory of Solidification Processing, Northwestern Polytechnical University, Xi'an 710072, China; School of Materials Science and Engineering, Northwestern Polytechnical University, Xi'an 710072, China;* orcid.org/0000-0002-2191-0930; Email: fuyichen@nwpu.edu.cn

Authors

Quan Tang − *State Key Laboratory of Solidification Processing, Northwestern Polytechnical University, Xi'an 710072, China; School of Materials Science and Engineering, Northwestern Polytechnical University, Xi'an 710072, China*

Longfei Guo − *State Key Laboratory of Solidification Processing, Northwestern Polytechnical University, Xi'an 710072, China; School of Materials Science and Engineering, Northwestern Polytechnical University, Xi'an 710072, China*

Tao Jin − *State Key Laboratory of Solidification Processing, Northwestern Polytechnical University, Xi'an 710072, China; School of Materials Science and Engineering, Northwestern Polytechnical University, Xi'an 710072, China*

Shuang Shan − *State Key Laboratory of Solidification Processing, Northwestern Polytechnical University, Xi'an 710072, China; School of Materials Science and Engineering, Northwestern Polytechnical University, Xi'an 710072, China*

Qiao Wang − *State Key Laboratory of Solidification Processing, Northwestern Polytechnical University, Xi'an 710072, China; School of Materials Science and Engineering, Northwestern Polytechnical University, Xi'an 710072, China*

Junpeng Wang − *State Key Laboratory of Solidification Processing, Northwestern Polytechnical University, Xi'an 710072, China; School of Materials Science and Engineering, Northwestern Polytechnical University, Xi'an 710072, China*

Bowei Pan − *State Key Laboratory of Solidification Processing, Northwestern Polytechnical University, Xi'an 710072, China; School of Materials Science and Engineering, Northwestern Polytechnical University, Xi'an 710072, China*

Zhen Li − *State Key Laboratory of Solidification Processing, Northwestern Polytechnical University, Xi'an 710072, China; School of Materials Science and Engineering, Northwestern Polytechnical University, Xi'an 710072, China*

Complete contact information is available at: https://pubs.acs.org/10.1021/acsomega.4c03637

Author Contributions

Q.T. and F.C. conceived the project, analyzed the data, and wrote the paper. Q.T. and Q.W. performed the catalyst preparation, catalytic testing, and physical characterization. T.J. and L.G. carried out atomistic simulation for this work. S.S., J.W., B.P., and Z.L. characterized the material structure with TEM and proposed the structure model. All authors discussed the results and commented on the manuscript.

Notes

The authors declare no competing financial interest.

https://doi.org/10.1021/acsomega.4c03637
ACS Omega 2024, 9, 45811−45821

■ ACKNOWLEDGMENTS

This work was supported by the National Natural Science Foundation of China (grant nos. 51874243, 51271148, and 50971100), the Research Fund of State Key Laboratory of Solidification Processing in China (grant no. 150-ZH-2016), the Aeronautic Science Foundation Program of China (grant no. 2012ZF53073), the Project of Transformation of Scientific and Technological Achievements of NWPU (grant no. 19−2017), and the Open Fund of State Key Laboratory of Advanced Technology for Materials Synthesis and Processing (Wuhan University of Technology grant no. 2018-KF-18). We thank the Analytical & Testing Center of Northwestern Polytechnical University for TEM and XPS characterizations.

■ REFERENCES

(1) Turner, J. A. Sustainable Hydrogen Production. *Science* **2004**, *305* (5686), 972−974. Deng, K.; Ren, T.; Xu, Y.; Liu, S.; Dai, Z.; Wang, Z.; Li, X.; Wang, L.; Wang, H. Crystalline core−amorphous shell heterostructures: epitaxial assembly of NiB nanosheets onto PtPd mesoporous hollow nanopolyhedra for enhanced hydrogen evolution electrocatalysis. *J. Mater. Chem. A* **2020**, *8* (18), 8927−8933. Huang, X.; Xu, X.; Li, C.; Wu, D.; Cheng, D.; Cao, D. Vertical CoP Nanoarray Wrapped by N,P-Doped Carbon for Hydrogen Evolution Reaction in Both Acidic and Alkaline Conditions. *Adv. Energy Mater.* **2019**, *9* (22), No. 1803970. Jang, S. W.; Dutta, S.; Kumar, A.; Hong, Y.-R.; Kang, H.; Lee, S.; Ryu, S.; Choi, W.; Lee, I. S. Holey Pt Nanosheets on NiFe-Hydroxide Laminates: Synergistically Enhanced Electrocatalytic 2D Interface toward Hydrogen Evolution Reaction. *ACS Nano* **2020**, *14* (8), 10578−10588.

(2) Schlapbach, L.; Züttel, A. Hydrogen-storage materials for mobile applications. *Nature* **2001**, *414* (6861), 353−358. Eberle, U.; Felderhoff, M.; Schüth, F. Chemical and Physical Solutions for Hydrogen Storage. *Angew. Chem., Int. Ed.* **2009**, *48* (36), 6608−6630.

(3) Yadav, M.; Xu, Q. Liquid-phase chemical hydrogen storage materials. *Energy Environ. Sci.* **2012**, *5* (12), 9698−9725. DOI: 10.1039/C2EE22937D Sordakis, K.; Tang, C.; Vogt, L. K.; Junge, H.; Dyson, P. J.; Beller, M.; Laurenczy, G. Homogeneous Catalysis for Sustainable Hydrogen Storage in Formic Acid and Alcohols. *Chem. Rev.* **2018**, *118* (2), 372−433. Nakajima, K.; Tominaga, M.; Waseda, M.; Miura, H.; Shishido, T. Highly Efficient Supported Palladium−Gold Alloy Catalysts for Hydrogen Storage Based on Ammonium Bicarbonate/Formate Redox Cycle. *ACS Sustainable Chem. Eng.* **2019**, *7* (7), 6522−6530.

(4) Grubel, K.; Jeong, H.; Yoon, C. W.; Autrey, T. Challenges and opportunities for using formate to store, transport, and use hydrogen. *J. Energy Chem.* **2020**, *41*, 216−224.

(5) Preuster, P.; Papp, C.; Wasserscheid, P. Liquid Organic Hydrogen Carriers (LOHCs): Toward a Hydrogen-free Hydrogen Economy. *Acc. Chem. Res.* **2017**, *50* (1), 74−85.

(6) Hellstén, P. P.; Salminen, J. M.; Jørgensen, K. S.; Nystén, T. H. Use of Potassium Formate in Road Winter Deicing Can Reduce Groundwater Deterioration. *Environ. Sci. Technol.* **2005**, *39* (13), 5095−5100. Jiang, J.; Wieckowski, A. Prospective direct formate fuel cell. *Electrochem. Commun.* **2012**, *18*, 41−43. An, L.; Chen, R. Direct formate fuel cells: A review. *J. Power Sources* **2016**, *320*, 127−139. Pan, B.; Chen, F.; Wang, J.; Tang, Q.; Guo, L.; Jin, T.; Peng, C.; An, L.; Chen, Y. PdAuAg Alloy Nanoparticles on Nickel Foam as Anode for Passive Air-Breathing Formate Fuel Cell. *J. Electrochem. Soc.* **2021**, *168* (6), No. 064519. Zhu, X.; Liang, S.; Chen, S.; Liu, X.; Li, R. Adsorption driven formate reforming into hydride and tandem hydrogenation of nitrophenol to amine over PdOx catalysts. *Catal. Sci. Technol.* **2020**, *10* (24), 8332−8338. Hwang, Y. J.; Kwon, Y.; Kim, Y.; Sohn, H.; Nam, S. W.; Kim, J.; Autrey, T.; Yoon, C. W.; Jo, Y. S.; Jeong, H. Development of an Autothermal Formate-Based Hydrogen Generator: From Optimization of Formate Dehydrogenation Conditions to Thermal Integration with Fuel Cells. *ACS Sustainable Chem. Eng.* **2020**, *8* (26), 9846−9856.

(7) Dong, Z.; Mukhtar, A.; Ludwig, T.; Akhade, S. A.; Kang, S.; Wood, B.; Grubel, K.; Engelhard, M.; Autrey, T.; Lin, H. Efficient Pd on carbon catalyst for ammonium formate dehydrogenation: Effect of surface oxygen functional groups. *Appl. Catal., B* **2023**, *321*, No. 122015.

(8) Choun, M.; Lee, J. Electro-oxidation of mixed reactants of ethanol and formate on Pd/C in alkaline fuel cells. *J. Energy Chem.* **2016**, *25* (4), 683−690. Zhang, N.; Chen, F.; Guo, L. Catalytic activity of palladium-doped silver dilute nanoalloys for formate oxidation from a theoretical perspective. *Phys. Chem. Chem. Phys.* **2019**, *21* (40), 22598−22610. Jin, T.; Chen, F.; Guo, L.; Tang, Q.; Wang, J.; Pan, B.; Wu, Y.; Yu, S. Pd4O3 Subsurface Oxide on Pd(111) Formed during Oxygen Adsorption-Induced Surface Reconstruction and Its Activity toward Formate Oxidation Reactions. *J. Phys. Chem. C* **2021**, *125* (35), 19497−19508.

(9) Tang, Q.; Chen, F.; Jin, T.; Guo, L.; Wang, Q.; Liu, H. Alloying in inverse CeO2/Pd nanoparticles to enhance the electrocatalytic activity for the formate oxidation reaction. *J. Mater. Chem. A* **2019**, *7* (40), 22996−23007. Wang, Q.; Chen, F.; Tang, Q.; Guo, L.; Gebremariam, T. T.; Jin, T.; Liu, H.; Kou, B.; Li, Z.; Bian, W. Transition from core-shell to janus segregation pattern in AgPd nanoalloy by Ni doping for the formate oxidation. *Appl. Catal., B* **2020**, *270*, No. 118861. Wang, Q.; Chen, F.; Tang, Q.; Guo, L.; Jin, T.; Pan, B.; Wang, J.; Li, Z.; Kou, B.; Bian, W. AgPdCo hollow nanospheres electrocatalyst with high activity and stability toward the formate electrooxidation. *Nano Res.* **2021**, *14* (7), 2268−2276. Wang, Q.; Chen, F.; Guo, L.; Jin, T.; Liu, H.; Wang, X.; Gong, X.; Liu, Y. Nanoalloying effects on the catalytic activity of the formate oxidation reaction over AgPd and AgCuPd aerogels. *J. Mater. Chem. A* **2019**, *7* (27), 16122−16135.

(10) Jin, Y.; Chen, F.; Jin, T.; Guo, L.; Wang, J. Mesoporous PdAgIr nanoalloys to catalyze formate oxidation with an unprecedentedly low onset potential. *J. Mater. Chem. A* **2020**, *8* (48), 25780−25790.

(11) Tang, Q.; Chen, F.; Wang, Q.; Jin, T.; Guo, L.; Wu, Y.; Yu, S.; Li, Z. Surface reconstruction of AgPdF and AgPd nanoalloys under the formate oxidation reaction. *J. Mater. Chem. A* **2021**, *9* (40), 23072−23084.

(12) Wei, D.; Shi, X.; Sponholz, P.; Junge, H.; Beller, M. Manganese Promoted (Bi)carbonate Hydrogenation and Formate Dehydrogenation: Toward a Circular Carbon and Hydrogen Economy. *ACS Cent. Sci.* **2022**, *8* (10), 1457−1463.

(13) Pan, B.; Shan, S.; Wang, J.; Tang, Q.; Guo, L.; jin, T.; Wang, Q.; Li, Z.; Usman, M.; Chen, F. Nickel-supported PdM (M = Au, Ag) nanodendrites as formate oxidation (electro)catalytic anodes for direct fuel cell and hydrogen generation in room temperature. *Nanoscale* **2023**, *15*, 7032−7043.

(14) Seh, Z. W.; Kibsgaard, J.; Dickens, C. F.; Chorkendorff, I.; Nørskov, J. K.; Jaramillo, T. F. Combining theory and experiment in electrocatalysis: Insights into materials design. *Science* **2017**, *355* (6321), No. eaad4998. Wang, X.; Zhu, Y.; Vasileff, A.; Jiao, Y.; Chen, S.; Song, L.; Zheng, B.; Zheng, Y.; Qiao, S.-Z. Strain Effect in Bimetallic Electrocatalysts in the Hydrogen Evolution Reaction. *ACS Energy Lett.* **2018**, *3* (5), 1198−1204. Nugraha, A. S.; Han, M.; Ashok, A.; Kang, Y.; Kim, J.; Alshehri, S. M.; Ahamad, T.; Bando, Y.; Yamauchi, Y. Synergistic mesoporous bimetallic gold-silver nanoparticles: Synthesis, structure, and superior electrocatalytic activity. *Nano Energy* **2023**, *116*, No. 108770. Han, M.; Kani, K.; Na, J.; Kim, J.; Bando, Y.; Ahamad, T.; Alshehri, S. M.; Yamauchi, Y. Retrospect and Prospect: Nanoarchitectonics of Platinum-Group-Metal-Based Materials. *Adv. Funct. Mater.* **2023**, *33* (44), No. 2301831. Nugraha, A. S.; Ashok, A.; Xia, W.; Miyata, H.; M Alshehri, S.; Ahamad, T.; Bando, Y.; Han, M.; Yamauchi, Y. Dealloying Strategies for Mesoporous AuCu Nanoparticles: Impact on Internal Metallic Structure and Electrocatalytic Performance *Small Struct.*, *5* 9 2400021 .

(15) Xie, C.; Yan, D.; Li, H.; Du, S.; Chen, W.; Wang, Y.; Zou, Y.; Chen, R.; Wang, S. Defect Chemistry in Heterogeneous Catalysis: Recognition, Understanding, and Utilization. *ACS Catal.* **2020**, *10* (19), 11082−11098. Tang, C.; Gong, P.; Xiao, T.; Sun, Z. Direct

https://doi.org/10.1021/acsomega.4c03637
ACS Omega 2024, 9, 45811−45821

electrosynthesis of 52% concentrated CO on silver's twin boundary. *Nat. Commun.* **2021**, *12* (1), No. 2139.
(16) Liu, C.; Shen, Y.; Zhang, J.; Li, G.; Zheng, X.; Han, X.; Xu, L.; Zhu, S.; Chen, Y.; Deng, Y.; Hu, W. Multiple Twin Boundary-Regulated Metastable Pd for Ethanol Oxidation Reaction. *Adv. Energy Mater.* **2022**, *12* (8), No. 2103505.
(17) Huang, W.; Johnston-Peck, A. C.; Wolter, T.; Yang, W.-C. D.; Xu, L.; Oh, J.; Reeves, B. A.; Zhou, C.; Holtz, M. E.; Herzing, A. A.; et al. Steam-created grain boundaries for methane C−H activation in palladium catalysts. *Science* **2021**, *373* (6562), 1518−1523.
(18) Liu, S.; Zhang, H.; Mu, X.; Chen, C. Surface reconstruction engineering of twinned Pd2CoAg nanocrystals by atomic vacancy inducement for hydrogen evolution and oxygen reduction reactions. *Appl. Catal., B* **2019**, *241*, 424−429.
(19) Sun, X.; Jiang, K.; Zhang, N.; Guo, S.; Huang, X. Crystalline Control of {111} Bounded Pt3Cu Nanocrystals: Multiply-Twinned Pt3Cu Icosahedra with Enhanced Electrocatalytic Properties. *ACS Nano* **2015**, *9* (7), 7634−7640. Lu, K. Stabilizing nanostructures in metals using grain and twin boundary architectures. *Nat. Rev. Mater.* **2016**, *1* (5), No. 16019. Zhang, Z.; Luo, Z.; Chen, B.; Wei, C.; Zhao, J.; Chen, J.; Zhang, X.; Lai, Z.; Fan, Z.; Tan, C.; et al. One-Pot Synthesis of Highly Anisotropic Five-Fold-Twinned PtCu Nanoframes Used as a Bifunctional Electrocatalyst for Oxygen Reduction and Methanol Oxidation. *Adv. Mater.* **2016**, *28* (39), 8712−8717.
(20) Wang, J.; Chen, F.; Jin, Y.; Guo, L.; Gong, X.; Wang, X.; Johnston, R. L. In situ high-potential-driven surface restructuring of ternary AgPd−Ptdilute aerogels with record-high performance improvement for formate oxidation electrocatalysis. *Nanoscale* **2019**, *11* (30), 14174−14185. Jin, Y.; Chen, F.; Guo, L.; Wang, J.; Kou, B.; Jin, T.; Liu, H. Engineering Two-Dimensional PdAgRh Nanoalloys by Surface Reconstruction for Highly Active and Stable Formate Oxidation Electrocatalysis. *ACS Appl. Mater. Interfaces* **2020**, *12* (23), 26694−26703. Pan, B.; Chen, F.; Kou, B.; Wang, J.; Tang, Q.; Guo, L.; Wang, Q.; Li, Z.; Bian, W.; Wang, J. Unexpectedly high stability and surface reconstruction of PdAuAg nanoparticles for formate oxidation electrocatalysis. *Nanoscale* **2020**, *12* (21), 11659−11671. Li, J.; Sharma, S.; Liu, X.; Pan, Y.-T.; Spendelow, J. S.; Chi, M.; Jia, Y.; Zhang, P.; Cullen, D. A.; Xi, Z.; et al. Hard-Magnet L10-CoPt Nanoparticles Advance Fuel Cell Catalysis. *Joule* **2019**, *3* (1), 124−135. Wang, X. X.; Swihart, M. T.; Wu, G. Achievements, challenges and perspectives on cathode catalysts in proton exchange membrane fuel cells for transportation. *Nat. Catal.* **2019**, *2* (7), 578−589. Kawaguchi, T.; Komanicky, V.; Latyshev, V.; Cha, W.; Maxey, E. R.; Harder, R.; Ichitsubo, T.; You, H. Electrochemically Induced Strain Evolution in Pt−Ni Alloy Nanoparticles Observed by Bragg Coherent Diffraction Imaging. *Nano Lett.* **2021**, *21* (14), 5945−5951. Passos, A. R.; Rochet, A.; Manente, L. M.; Suzana, A. F.; Harder, R.; Cha, W.; Meneau, F. Three-dimensional strain dynamics govern the hysteresis in heterogeneous catalysis. *Nat. Commun.* **2020**, *11* (1), No. 4733.
(21) Guo, L.; Chen, F.; Jin, T.; Liu, H.; Zhang, N.; Jin, Y.; Wang, Q.; Tang, Q.; Pan, B. Surface reconstruction of AgPd nanoalloy particles during the electrocatalytic formate oxidation reaction. *Nanoscale* **2020**, *12* (5), 3469−3481.
(22) Divins, N. J.; Angurell, I.; Escudero, C.; Pérez-Dieste, V.; Llorca, J. Influence of the support on surface rearrangements of bimetallic nanoparticles in real catalysts. *Science* **2014**, *346* (6209), 620−623. Lei, Y.; Zhao, H.; Rivas, R. D.; Lee, S.; Liu, B.; Lu, J.; Stach, E.; Winans, R. E.; Chapman, K. W.; Greeley, J. P.; et al. Adsorbate-Induced Structural Changes in 1−3 nm Platinum Nanoparticles. *J. Am. Chem. Soc.* **2014**, *136* (26), 9320−9326. Eren, B.; Zherebetskyy, D.; Patera, L. L.; Wu, C. H.; Bluhm, H.; Africh, C.; Wang, L.-W.; Somorjai, G. A.; Salmeron, M. Activation of Cu(111) surface by decomposition into nanoclusters driven by CO adsorption. *Science* **2016**, *351* (6272), 475−478. Grosse, P.; Yoon, A.; Rettenmaier, C.; Herzog, A.; Chee, S. W.; Roldan Cuenya, B. Author Correction: Dynamic transformations of cubic copper catalysts during CO2 electroreduction and its impact on catalytic selectivity. *Nat. Commun.* **2021**, *12* (1), No. 7329. Yan, G.; Tang, Y.; Li, Y.; Li, Y.; Nguyen, L.; Sakata, T.; Higashi, K.; Tao, F. F.; Sautet, P. Reaction product-driven restructuring and assisted stabilization of a highly dispersed Rh-on-ceria catalyst. *Nat. Catal.* **2022**, *5* (2), 119−127.
(23) Tao, F.; Grass, M. E.; Zhang, Y.; Butcher, D. R.; Aksoy, F.; Aloni, S.; Altoe, V.; Alayoglu, S.; Renzas, J. R.; Tsung, C.-K.; et al. Evolution of Structure and Chemistry of Bimetallic Nanoparticle Catalysts under Reaction Conditions. *J. Am. Chem. Soc.* **2010**, *132* (25), 8697−8703.
(24) Jiang, B.; Zhang, X.-G.; Jiang, K.; Wu, D.-Y.; Cai, W.-B. Boosting Formate Production in Electrocatalytic CO2 Reduction over Wide Potential Window on Pd Surfaces. *J. Am. Chem. Soc.* **2018**, *140* (8), 2880−2889.
(25) Hÿtch, M.; Snoeck, E.; Kilaas, R. Quantitative measurement of displacement and strain fields from HREM micrographs. *Ultramicroscopy* **1998**, *74* (3), 131−146.
(26) Du, W.; Wang, Q.; Saxner, D.; Deskins, N. A.; Su, D.; Krzanowski, J. E.; Frenkel, A. I.; Teng, X. Highly Active Iridium/Iridium−Tin/Tin Oxide Heterogeneous Nanoparticles as Alternative Electrocatalysts for the Ethanol Oxidation Reaction. *J. Am. Chem. Soc.* **2011**, *133* (38), 15172−15183. Wang, J.; Chen, F.; Jin, Y.; Lei, Y. Dilute Au-Containing Ag Nanosponges as a Highly Active and Durable Electrocatalyst for Oxygen Reduction and Alcohol Oxidation Reactions. *ACS Appl. Mater. Interfaces* **2018**, *10* (7), 6276−6287.
(27) Tang, Q.; Guo, L.; Jin, T.; Shan, S.; Wang, Q.; Wang, J.; Pan, B.; Li, Z.; Chai, Y.; Chen, F. Stable Strain State of Single-Twinned AgPdF Nanoalloys under Formate Oxidation Reaction. *Small Struct.* **2023**, *4* (10), No. 2300110.
(28) Kitchin, J. R.; Reuter, K.; Scheffler, M. Alloy surface segregation in reactive environments: First-principles atomistic thermodynamics study of ${\mathrm{Ag}}_{3}\mathrm{Pd}(111)$ in oxygen atmospheres. *Phys. Rev. B* **2008**, *77* (7), No. 075437.
(29) Bian, W.; Chen, F.; Li, Z.; Kou, B.; Jin, T.; Guo, L.; Tang, Q. Surface phase stability of PdAg core-shell nanoalloys in oxidizing atmospheres and its relevance to surface atomic charge. *J. Alloys Compd.* **2021**, *869*, No. 159345.
(30) Suntivich, J.; Xu, Z.; Carlton, C. E.; Kim, J.; Han, B.; Lee, S. W.; Bonnet, N.; Marzari, N.; Allard, L. F.; Gasteiger, H. A.; et al. Surface Composition Tuning of Au−Pt Bimetallic Nanoparticles for Enhanced Carbon Monoxide and Methanol Electro-oxidation. *J. Am. Chem. Soc.* **2013**, *135* (21), 7985−7991. Tao, F. F.; Crozier, P. A. Atomic-Scale Observations of Catalyst Structures under Reaction Conditions and during Catalysis. *Chem. Rev.* **2016**, *116* (6), 3487−3539. Kou, B.; Chen, F.; Li, Z.; Bian, W.; Guo, L.; Jin, T. Surface phase stability of surface segregated AgPd and AgCu nanoalloys in an oxygen atmosphere. *Appl. Phys. A* **2021**, *127* (6), No. 406.
(31) Selvam, N. C. S.; Du, L.; Xia, B. Y.; Yoo, P. J.; You, B. Reconstructed Water Oxidation Electrocatalysts: The Impact of Surface Dynamics on Intrinsic Activities. *Adv. Funct. Mater.* **2021**, *31* (12), No. 2008190.
(32) Liu, Y.; Wu, J.; Hackenberg, K. P.; Zhang, J.; Wang, Y. M.; Yang, Y.; Keyshar, K.; Gu, J.; Ogitsu, T.; Vajtai, R.; et al. Self-optimizing, highly surface-active layered metal dichalcogenide catalysts for hydrogen evolution. *Nat. Energy* **2017**, *2* (9), No. 17127. Wang, Y.; Wang, G.; Li, G.; Huang, B.; Pan, J.; Liu, Q.; Han, J.; Xiao, L.; Lu, J.; Zhuang, L. Pt−Ru catalyzed hydrogen oxidation in alkaline media: oxophilic effect or electronic effect? *Energy Environ. Sci.* **2015**, *8* (1), 177−181.

https://doi.org/10.1021/acsomega.4c03637
ACS Omega 2024, 9, 45811−45821